RSC Advances

ROYAL SOCIETY OF CHEMISTRY

www.rsc.org/advances

Table of contents

New approach to improve the conductivity of apatite-type lanthanum germanate $La_{9.33}Ge_6O_{26}$ as electrolyte for IT-SOFCs

Guangchao Yin, Hong Yin, Meiling Sun, Linhong Zhong, Junkai Zhang, Ridong Cong, Wei Gao*

and Qiliang Cui

Graphical abstract:

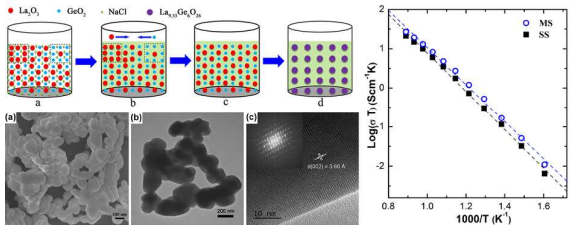

Text: $La_{9.33}Ge_6O_{26}$ pellets synthesized by molten-salt method exhibit higher conductivity owing to the high density and the avoidance of La_2GeO_5.

Cite this: DOI: 10.1039/c0xx00000x

www.rsc.org/xxxxxx

PAPER

New approach to improve the conductivity of apatite-type lanthanum germanate $La_{9.33}Ge_6O_{26}$ as electrolyte for IT-SOFCs

Guangchao Yin, Hong Yin, Meiling Sun, Linhong Zhong, Junkai Zhang, Ridong Cong, Wei Gao* and Qiliang Cui

Received (in XXX, XXX) Xth XXXXXXXXX 20XX, Accepted Xth XXXXXXXXX 20XX
DOI: 10.1039/b000000x

Apatite-type $La_{9.33}Ge_6O_{26}$ powders have been successfully synthesized by facile molten-salt synthesis method, using NaCl as eutectic salt. The morphology, structure and phase composition of the powders were examined. The results demonstrated that the apatite-type $La_{9.33}Ge_6O_{26}$ powders are homogeneous, nano-size, non agglomerated and well crystallized particles, which are favorable to obtain the highly dense pellets. Compared with the conventional methods, the dense pellets have been successfully sintered at a relatively lower temperature of 1100 °C, which availably inhibit the vaporization of GeO_2. The pellets exhibit a higher conductivity with a value of 2.4×10^{-2} S cm^{-1} at 850 °C, due to the high density and the avoidance of impurity La_2GeO_5. The main problems such as Ge volatility, agglomeration and crystallinity encountered in the conventional methods have been effectively solved via the molten-salt synthesis method. In addition, the related mechanism is also discussed in present paper.

Introduction

The investigations of apatite-type lanthanum silicates/germanates (ATLS/ATLG) as novel electrolyte materials for intermediate temperature solid oxide fuel cells (IT-SOFCs) have gained considerable interest owing to their clean energy conversion, high energy efficiency and potential use for developing fuel cell devices [1-14]. In contrast to a vacancy mechanism commonly observed for the fluorite- and perovskite-type oxide-ion conductors, such as doped ZrO_2 (e.g. YSZ) [15, 16] and doped $LaGaO_3$ (e.g. LSGM) [17], ATLS/ATLG has a unique interstitial conduction mechanism leading to a higher ionic conductivity at intermediate temperature. Moreover, ATLG is even more superior to ATLS, in terms of higher conductivities at similarly intermediate temperatures (500-800 °C), lower synthesis/sintering temperatures and higher oxygen interstitial contents achievable [18]. Up to now, researches have been extensively focused on ATLS [19-22], while, ATLG has not attracted much attention as it deserved because of the difficulty of its preparation due to the Ge loss.

Previous investigations indicated that Ge will have an obvious loss due to the high mobility of Ge^{4+} under high synthesis/sintering temperatures (> 1150 °C), that is difficult to be overcome in the conventional solid-state synthesis (SSS) method [23-25]. Generally in SSS process, the high temperature and long dwelling time are indispensable to obtain highly dense product with well crystallinity for conductivity measurements. On the other hand, such high temperature inevitably causes the loss of Ge related to the volatility of GeO_2, unfortunately resulting in the formation of impurity (La_2GeO_5) with the increase of La:Ge ratio. It has been reported that the introduction of La_2GeO_5 will reduce the conductivity of the as-prepared product [26]. Thus, it is not ideal to involve high temperature during the synthesis process, despite it profits to obtain well-crystallize and dense product. Consequently, a reduced sintering temperature is urgently needed for maintaining the La:Ge ratio meanwhile other structural characteristics are optimized.

Recently, great efforts have been devoted to lowering the sintering temperature by the usage of alternative synthesis routes to fabricate ATLG, such as ball-mill method, sol-gel auto-combustion method and so on, yet little improvement has been achieved. Ball-mill method successfully lowered the synthesis temperature, but the poor crystallinity of the samples hindered their conductive measurements [27]. Although successful in the preparation of high quality samples, sol-gel auto-combustion route requires high temperature treatments to achieve the dense pellets for conductive measurements [28]. Taking both points into account, searching alternative methods consequently becomes essential for the purpose of fundamental point of view as well as the potential applications of ATLG.

Therefore, it is the aim of the present paper to demonstrate a novel route for preparing ATLG as electrolyte materials for IT-SOFCs by using molten-salt synthesis (MSS) method. This method has been adopted by Li and his co-workers to fabricate ATLS [29, 30], by which the use of NaCl as eutectic salt has been typically involved at the synthesis temperatures as low as 900 °C. This synthesis temperature is significantly lower than the generally reported temperatures for preparing ATLG, hence it is expected to effectively solve the Ge volatility problem when employing MSS method. In addition, as compared to the traditional SSS method, MSS method exhibits advantages of simple process, clean, repeatability of the salt and also better

crystal morphology and homogeneity of the obtained powder product, which is more applicable from the industrial point of view.

Experimental section

Starting reactant powders of lanthanum oxide (La_2O_3, 99.99%, Sinopharm Chemical Reagent Co.Ltd) and germanium dioxide (GeO_2, 99.99%, Sinopharm Chemical Reagent Co.Ltd) were weighed in the proper composition of $La_{9.33}Ge_6O_{26}$. Hygroscopic lanthanum oxide was precalcined at 1000 °C for 2 h in order to remove lanthanum hydroxide and/or oxycarbonate phases to obtain the appropriate amount of La_2O_3. Sodium chloride (NaCl, 99%, Sinopharm Chemical Reagent Co.Ltd) was taken as the eutectic salt, and the mass ratio of reactants ((La_2O_3 and GeO_2) to NaCl were fixed to be 1:3. This mass ratio is determined through a large number of experiments, and the same mass ratio has been adopted by Li and his co-workers in the fabrication of apatite-type lanthanum silicates [29, 30]. The intimately mixed powders (La_2O_3, GeO_2 and NaCl) were first ball milled in ethanol medium at a speed of 400 rpm for 8 h, dried, ground and sifted to avoid agglomerated powders. The sifted powders were calcined at 750 °C, 800 °C and 900 °C for 4 h, respectively. The as-synthesized powders were washed and filtered repeatedly with de-ionized water to remove free NaCl until there was no appearance of white precipitate in the filtrate by adding $AgNO_3$ solution. Then the as-synthesized powders still were washed and filtered for several times with de-ionized water to keep the powders pure. Finally $La_{9.33}Ge_6O_{26}$ powders were obtained by drying the samples at 110 °C for 12 h. The final powders were sieved and isostatic cool pressed under 100 MPa into pellets, and then sintered at 1100 °C for 2 h with a heating rate of 10 °C min^{-1}. For comparison, a powder was synthesized by the SSS method at 1100 °C for 4 h and the final pellets were sintered at 1300 °C for 2 h.

In order to study the synthesis process for optimizing the synthesis temperature, thermo gravimetry/differential thermal analysis (TG/DTA; LINSEIS STA PT 1600) were performed on the sifted powders of mixtures from the room temperature to 1200 °C with a heating rate of 10 °C min^{-1}. Moreover, TG/DTA experiments of GeO_2 powders were also performed with the similar experimental parameters to investigate the Ge volatility condition for optimizing the sintering temperature. Phase identification, crystallinity and crystal structure of the powders were checked using X-ray diffraction (XRD; Shimadu XRD-6000). The measurements were done using Cu-Kα radiation (λ= 1.5418 Å) in the 2θ range of 20-60°, with a step size of 0.02° and counting time of 2 s. The morphology observation and the structural characterization were conducted with field emission scanning electron microscope (FESEM; JEOL JSM-6700F) and high-resolution transmission electron microscopy (HRTEM; JEOL JEM-2200FS). Energy dispersive X-ray analysis (EDX) of the of $La_{9.33}Ge_6O_{26}$ powders was performed with an EDAX Genesis 2000 system (FEI Inc) installed on the XL 30 ESEM imaging instrument. The electrochemical impedance spectroscopy (ESI) measurements were conducted in air using *ac* impedance spectroscopy (Solartron 1260 frequency response analyzer). Electrodes were prepared by coating both plate faces with a platinum paste, which were then heated at 1000 °C for 30 min to decompose the paste and harden the Pt residue. Impedance measurement were performed at a 50 °C interval in air between 350 °C and 850 °C over frequency range of 1 Hz to 10 MHz, and followed by analyzing these results using Z-View software.

Results and Discussion

The obtained TG/DTA curves for mixture of La_2O_3, GeO_2 and NaCl are shown in Figure 1. The curves can be divided into two regions. From 200 °C to 800 °C, the slight weight loss is approximately 2 wt.% in TG curve, in the meanwhile, two wide endothermic peaks in the DTA curve can be found because of the dehydration and evaporation of the surviving water and carbon dioxide in mixture [31]. Above 800 °C, there is a significant weight loss (~ 45 wt.%) revealed by TG curve. Noticeably, two endothermic peaks occur at nearly 805 °C and 860 °C, respectively. The first endothermic peak (at nearly 805 °C) should be attributed to the fusion of eutectic NaCl. The other endothermic peak (at nearly 860 °C) is considered to be related to the complete formation of apatite phase, which will be clarified in more detail on the basis of the corresponding XRD patterns in following part. In addition, the TG/DTA curves of the GeO_2 powders in the temperature range of 900-1200 °C are shown in the inset of Figure 1, in order to more distinctly display the GeO_2 volatility condition for optimizing the sintering temperature. There is a significant endothermic peak at ~ 1120 °C in DTA curve, accompanied with an abrupt reduction of TG curve, which should be attributed to melting of GeO_2. Because of the volatilization of GeO_2 at higher temperature, the TG curve shows an obvious Ge loss between 1120 °C and 1200 °C. Therefore, the optimal sintering temperature should be below 1120 °C to avoid the significant Ge loss.

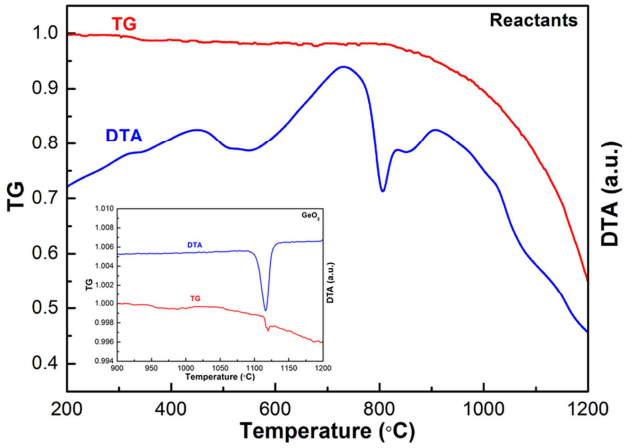

Fig. 1 The TG/DTA curves of the sifted powders of mixtures (La_2O_3, GeO_2 and NaCl) among 200-1200 °C at 10 °C min^{-1} in air. The inset is the TG/DTA curves of GeO_2 among 900-1200 °C.

To determine the endothermic peak at nearly 860 °C and optimize the synthesis temperature, the simultaneous XRD measurements of the mixed powders at different sintering temperature (750 °C, 800 °C and 900 °C for 4 h) were carried, and the results are given in Figure 2. At 750 °C, the pattern displays an apatite phase trend with obvious precursors and impurities. Then the pattern of 800 °C displays an apatite phase, but some precursors and impurities also can be observed. When

the temperature increases to 900 °C, the pattern can be indexed to a pure apatite phase with no impurity according to JCPDS-0043. The strong and sharp diffraction peaks suggest that the as-prepared powders are well crystallized. The XRD patterns distinctly confirm the above consideration that the endothermic peak occurred at nearly 860 °C is related with the complete formation of apatite phase. Furthermore, the XRD patterns also demonstrate that the melting-salt environment can promote the formation of apatite phase. Noticeably, the apatite phase begins to form with the melt of NaCl, and finally achieving the complete apatite phase when NaCl is completely melting. Under the effect of melting-salt environment, we have successfully synthesized apatite-type $La_{9.33}Ge_6O_{26}$ powders at 900 °C for 4h, which is lower at least 200 °C than that of SSS method. Moreover, the $La_{9.33}Ge_6O_{26}$ powders synthesized by molten-salt method display a better crystallinity than that synthesized by solid-state method (see Figure 2), despite of the lower synthesis temperature. Simultaneously the lower synthesis temperature effectively inhibits Ge volatility and provides a favorable basis for the further sintering of pellets.

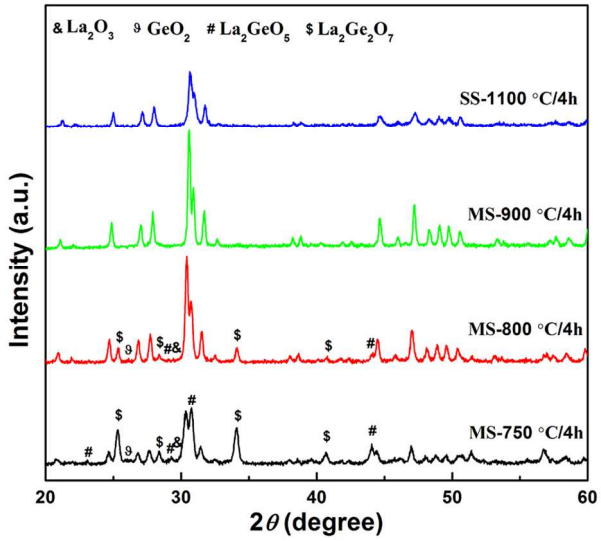

Fig. 2 XRD patterns of the powders synthesized by molten-salt method at 750 °C, 800 °C, and 900 °C for 4 h, respectively. And the XRD pattern of the powders synthesized by solid-state method at 1100 °C for 4 h.

Here, for comparing the cell values of $La_{9.33}Ge_6O_{26}$ powders synthesized by MSS method at 900 °C for 4 h (P-MS) and that synthesized by SSS method at 1100 °C for 4 h (P-SS), we refined the corresponding XRD patterns by the Rietveld refinements. A structural model with the $P6_3/m$ space group was adopted for the refinement, and the structural parameters were taken from the model by L. Leon-Reina et al [32]. This refined structural model gives good refinements to the XRD patterns, as shown in Figure S1. The relevant Rietveld refinement parameters are R_{wp}= 8.1%, R_p= 7.4% for P-MS; R_{wp}= 8.4%, R_p= 7.7% for P-SS, which further confirm that the results from Rietveld refinements are reasonable [33, 34]. The crystal parameters are a= 9.9189(2) Å, c= 7.2815(2) Å, V= 620.41(2) Å^3 for P-MS; a= 9.919(21) Å, c= 7.282(1) Å, V= 620.6(2) Å^3 for P-SS. The crystal parameters of P-MS are almost same with that of P-SS, which indirectly indicates the inexistence of Na in the samples prepared by MSS method [30].

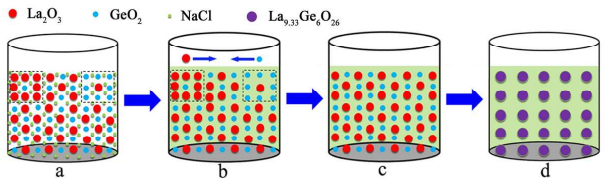

Fig. 3 Schematic illustration of reaction process in MSS method.

To more distinctly clarify the effect of melting environment, a schematic illustration of reaction process is shown in Figure 3. Similar to SSS method, the reactants and salt initially mix together with some partial inhomogeneous distributions, such as excessive La_2O_3 and excessive GeO_2, as shown in Figure 3a. In general, these partial inhomogeneous distributions will result in the formation of impurities in SSS method owing to the weak diffusivity during reaction process, the chemical reactions are shown as equation (1) and (2). In contrast to SSS, a melting-salt environment can be brought via the melt of molten-salt in MSS method, which is advantageous to promote the diffusivity of reactants. The reactants dispersing in the melting-salt environment can rapidly rearrange and diffuse, finally reaching a homogeneous distribution, as shown in Figure 3b and 3c. As a result, the formations of impurities are avoided, and the pure apatite-type $La_{9.33}Ge_6O_{26}$ powders are synthesized by the chemical reaction equation (3). Furthermore, owing to the homogeneous mixing of La_2O_3, GeO_2 and NaCl, the reaction can reach the atomic/molecule-scale in MSS method compared with the contact reaction in SSS method, which can effectively decrease the reaction temperature, shorten reaction time and improve reaction quality. Therefore, the well crystallized powders can be obtained at a lower synthesis temperature of 900 °C. In addition, different to coarse particle size with wide distribution and obvious particles agglomeration, the particles obtained by MSS method will be homogeneous and non agglomerated, because the growing particles are surrounded by the molten salts in reaction process (Figure 3d), which can be confirmed by the FESEM and TEM images.

$$La_2O_3 + GeO_2 = La_2GeO_5 \quad (1)$$

$$La_2O_3 + 2GeO_2 = La_2Ge_2O_7 \quad (2)$$

$$(9.33/2)La_2O_3 + 6GeO_2 = La_{9.33}Ge_6O_{26} \quad (3)$$

The FESEM image of $La_{9.33}Ge_6O_{26}$ powders is shown in Figure 4(a), which illustrates the powders are homogeneous and nano-size particles. The detailed structure of the powders has been further investigated by TEM (Figure 4(b)) and HRTEM (Figure 4(c)). It can be seen clearly that the powders are homogeneous, nano-size and non agglomerated particles, and they occupy a narrow size range with the average particle size of around 200 nm, which are consistent with the FESEM observation. The HRTEM image demonstrates that the as-prepared powders possess high crystallinity and have no visible defects and dislocations. The observed 3.66 Å spacing fringe is consistent with the (002) lattice plane of hexagonal apatite-type

$La_{9.33}Ge_6O_{26}$. Furthermore, the corresponding SAED pattern which is shown in the top-left inset of Figure 4(c) reveals that the powders are single crystals in nature. The homogeneous, non agglomerated and well crystallized powders are favorable for the preparation of dense and well crystallized pellets. In addition, the EDX spectrum of $La_{9.33}Ge_6O_{26}$ powders obtained by MSS method is shown in Figure 5. It can seen clearly that there are only La, Ge and O three elements in the samples except C element induced by the conductive adhesive, which gives direct evidence for the inexistence of Na in the samples prepared.

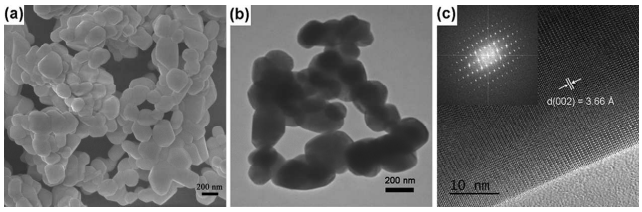

Fig. 4 SEM (a), TEM (b) and HRTEM (c) images of $La_{9.33}Ge_6O_{26}$ powders obtained by MSS method at 900 °C for 4 h. And the inset in (c) shows the corresponding SAED pattern.

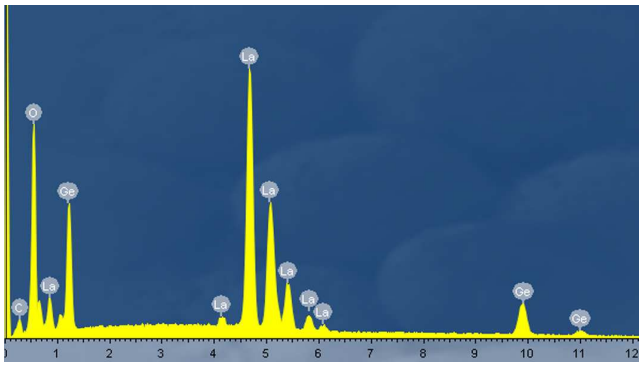

Fig. 5 EDX spectrum of $La_{9.33}Ge_6O_{26}$ powders obtained by MSS method at 900 °C for 4 h.

In order to measure the conductivity, the dense and well crystallized pellets are necessary to be obtained. Generally, the high temperature (≥1300 °C) and long dwelling time are needed to obtain the ideal pellets, because of the weak dispersity and bad crystallinity [35, 36]. However, the high sintering temperature will cause the obvious Ge loss owing to the volatility of GeO_2, which can be clearly seen in the TG/DTA curves of the GeO_2 powders (see the inset of Figure 1). In our work, on the basis of the homogeneous and well crystallized powders, the ideal pellets can be obtained at the relatively lower temperature. The dense pellets sintered at 1100 °C have showed high density, and the relative density of that has reached to ~ 90% measuring by Archimedean method. Consistent with the density, SEM image of the cross-section of pellets shown in Figure 6 displayed that the pellets are very dense, which could satisfy the application in SOFCs. Moreover, the cross-section is partially uneven, which leads to the "waves" observed in the microstructure picture. Noticeably, the temperature of 1100 °C is lower than the melting temperature of GeO_2 (about 1120 °C shown in the inset of Figure 1), which can availably inhibit the volatility of GeO_2 to keep the pure sample, as shown in Figure 7. The strong and sharp diffraction peaks suggest that the pellets are well crystallized. However, the compared pellets sintered by SSS method at 1300 °C for 2 h displayed an impurity phase of La_2GeO_5, which should be attributed to the high sintering temperature that causes the obvious Ge loss. As described in the introduction, the Ge loss will lead to the increase of La:Ge ratio, resulting in the appearance of impurity La_2GeO_5 that is very disadvantageous to the conductivity [26]. Herein, we suppose the pellets prepared by the homogeneous and well crystallized powders obtained by melt-salt method will exhibit a better conductivity.

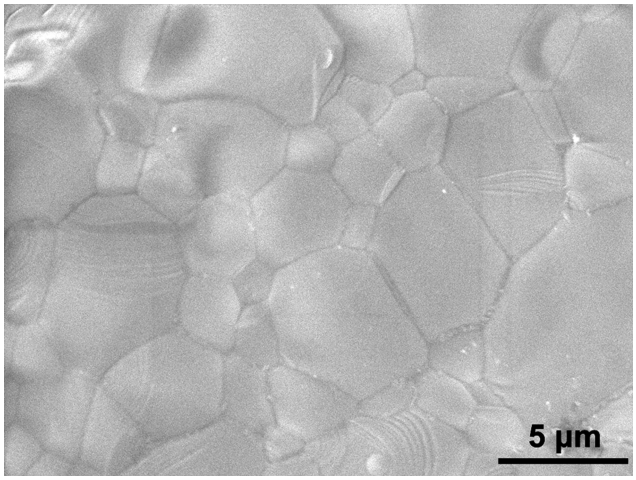

Fig. 6 SEM of the cross-section of pellets prepared by the powders obtained by MSS method at 1100 °C for 2 h.

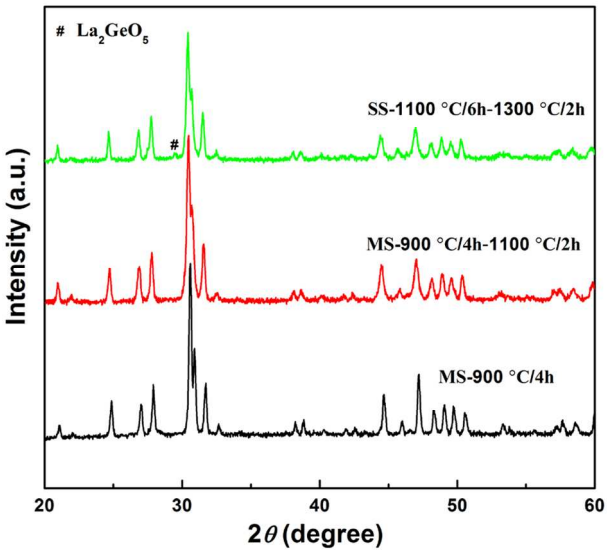

Fig. 7 XRD patterns of $La_{9.33}Ge_6O_{26}$ powders calcined at 900 °C for 4 h and the corresponding pellets sintered at 1100 °C for 2 h, and the compared pellets sintered by SSS method at 1300 °C for 2 h.

The conductivity is measured by *ac* impedance in the temperature range of 350-850 °C with an increment of 50 °C in air, and the obtained complex impedance spectrum measured at 350°C, 550 °C and 750 °C are shown in Figure 8. In a typical *ac* impedance measurement, the complex impedance of a sample as a function of frequency is measured. Generally, in polycrystalline specimens, two independent semicircular arcs from high frequency to low frequency correspond to the conduction across the bulk (R_{bulk}) and grain boundaries (R_{gb}), and an impedance response corresponding to electrode (R_{elec}) that appears as a straight line in the lower frequency range. In order to distinguish the contributions of bulk, grain boundary and electrode, the corresponding contributions have been managed using the Z-View software by modeling the impedance spectrum with the equivalent circuit including four serial R_i and $(CPE)_i$ parallels (*i* is *bulk* for bulk, *gb* for grain boundary, *total* for bulk and grain boundary and *elec* for electrode). The corresponding equivalent circuit is displayed as the insets. At the low measuring temperature of 350 °C, the the *ac* impedance plots exhibit two semicircles and a straight line. The fitting leads to $CPE_{bulk}\approx 8.0\times10^{-12}$ Fcm^{-1}, $CPE_{gb}\approx 2.3\times10^{-10}$ Fcm^{-1} and $CPE_{elec}\approx 2.1\times10^{-6}$ Fcm^{-1}, thus both semicircles are ascribed to the contributions of bulk and grain boundary, respectively, and the strait line is ascribed to the contribution of electrode. Since the grain semicircle and grain-boundary semicircle represent the blocking effects of the grain and grain/grain interfacial contact boundary for oxide ions, respectively. As the temperature increased, the grain and grain-boundary blocking effects progressively became smaller and eventually negligible. As a result the semicircles corresponding to the grain and grain boundary contribution progressively became smaller and eventually disappeared in *ac* impedance spectra. As shown the *ac* impedance plots measured at 550 °C, the contribution from the bulk process has not been observed, so which displayed two semicircles corresponding to the contribution of grain boundary and electrode ($CPE_{gb}\approx 6.8\times10^{-10}$ Fcm^{-1}, $CPE_{elec}\approx 7.3\times10^{-6}$ Fcm^{-1}), respectively. At the higher temperature of 750 °C, the contribution of the grain boundary process also has not been observed, and the only semicircle is ascribed to the contribution of electrode ($CPE_{elec}\approx 1.9\times10^{-5}$ Fcm^{-1}). Disappearance of the semicircle corresponding to grain boundary contribution implies that each polycrystalline region separated by the grain/grain interfacial contact boundary behaves like a single crystal with T ≥ 750 °C. [37, 38].

The corresponding conductivity is converted by the resistance R_{total} (R_{bulk}+ R_{gb}) using the equation (4), and the activation energy is calculated by the Arrhenius equation (5):

$$\sigma = l/(R_{total}*S) \quad (4)$$

$$\sigma = \sigma_0*\exp[-E_a/(k*T)]/T \quad (5)$$

where l , S, σ, σ_0, E_a and T are, respectively, the sample thickness, the electrode area of the sample surface, the conductivity, pre-exponential factor, activation energy, Boltzmann constant, and absolute temperature.

Both the total conductivities of pellets prepared by MSS and SSS method at different temperatures are plotted in Arrhenius plots (Figure 8). As shown, the pellets obtained by MSS method display an evidently higher conductivity than that obtained by SSS method. $La_{9.33}Ge_6O_{26}$ pellets obtained by MSS method exhibits an excellent conductivity with the value reaching to 2.4×10^{-2} S cm^{-1} at 850 °C ($\sigma_{850\ °C}$ =2.4×10^{-2} S cm^{-1}), which is higher than the same composition reported by other investigators [26-28, 35, 36]. It should be attributed to the high density and the avoidance of impurity La_2GeO_5. In previous investigations, the pellets prepared by SSS method is difficult to reach a high density despite of the relatively high sintering temperature, for example, $La_{9.33}Ge_6O_{26}$ pellets obtained at 1150 °C for 14 h can only reach a low density with a value of 61.3% , resulting in a

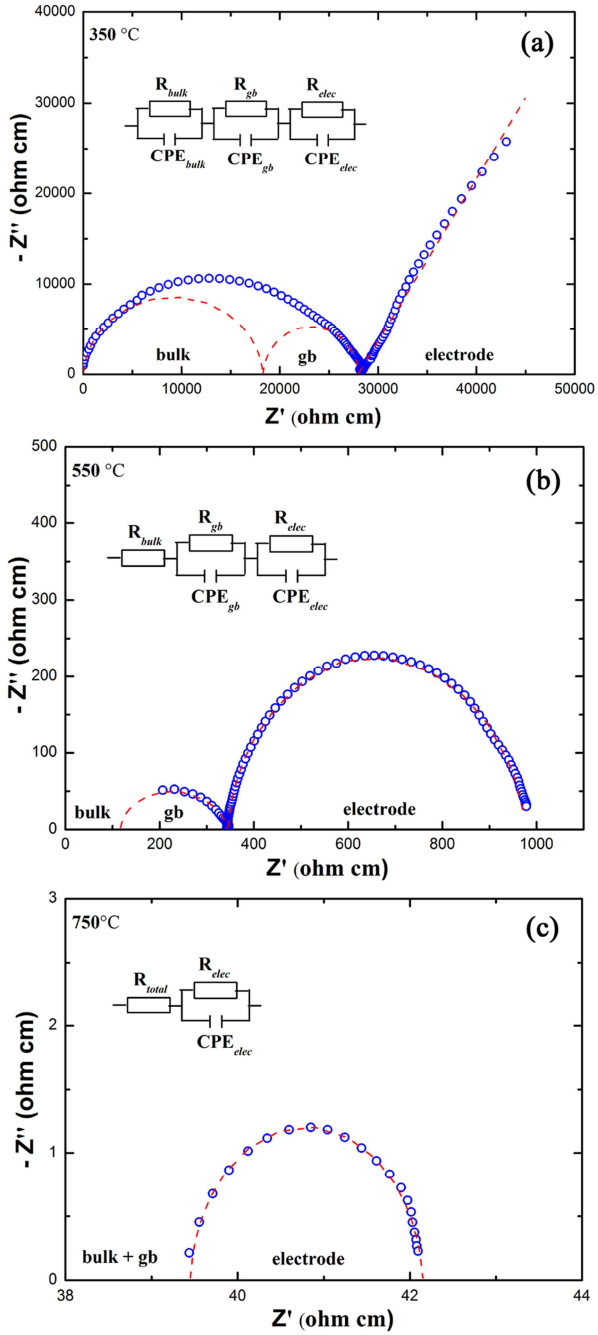

Fig. 8 The ac impedance spectra measured at 350 °C (a), 550 °C (b) and 750 °C (c) for the La9.33Ge6O26 pellets sintered at 1100 °C for 2 h, and the corresponding schematic equivalent circuits

low conductivity ($\sigma_{800\ °C}$ =3.1×10^{-3} S cm^{-1}) [26]. The further extended sintering study indicated $La_{9.33}Ge_6O_{26}$ pellets obtained at 1350 °C for 44 h can reach a high density with a value of ~ 90%, but the high sintering temperature and long dwelling time leaded to the formation of impurity La_2GeO_5 that is disadvantageous to conductivity, also resulting in a relatively low conductivity ($\sigma_{800\ °C}$ =1.0×10^{-2} S cm^{-1}) [35]. In our work, on the basis of the homogeneous and well crystallized powders, the density of pellets sintered at 1100 °C for 2 h has reached to ~ 90%, which could satisfy the application in SOFCs. Simultaneously, the disadvantageous effect of impurity La_2GeO_5 on conductivity has been overcome, because the low sintering temperature availably inhibits the vaporization of GeO_2. Therefore, the pellets obtained by MSS method can exhibit a higher total conduction value, due to the high density and the absence of the low conductive phase La_2GeO_5. In addition, the corresponding activation energy calculated by the Arrhenius equation is ~ 0.94 eV for MSS method, which is lower than that of the same composition reported by other investigators. The decrease in activation energy should be attributed to the avoidance of La_2GeO_5 according to the previous studies [26, 35, 36]. Generally, the decrease in activation energy can lead an increase in conductivity [39].

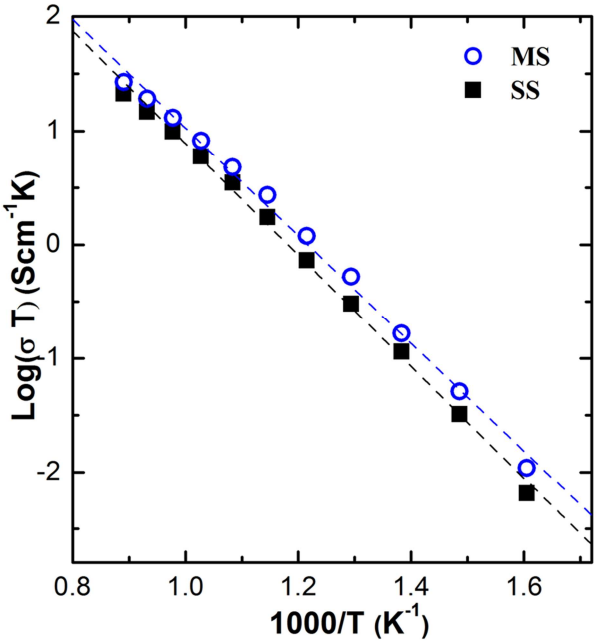

Fig. 9 The Arrhenius plots for the conductivity of $La_{9.33}Ge_6O_{26}$ pellets sintered by MSS at 1100 °C and the compared pellets sintered by SSS method at 1300 °C.

Conclusions

In summary, we have successfully synthesized apatite-type $La_{9.33}Ge_6O_{26}$ powders at 900 °C via molten-salt synthesis method, using NaCl as eutectic salt. The synthesized powders display the homogeneous, nano-size, non agglomerated and well crystallized characters, which is attributed to the effect of melting-salt environment that can promote the diffusivity of reactants. On the basis of good powders, the high dense pellets have been obtained at lower temperature of 1100 °C. The lower synthesizing/sintering temperature effectively inhibit the Ge loss, thus the impurity La_2GeO_5 has been successfully avoided. Without the disadvantageous effect of impurity La_2GeO_5 on conductivity, the dense $La_{9.33}Ge_6O_{26}$ pellets exhibit an ideal conductivity with a value of 2.4×10^{-2} S cm^{-1} at 850 °C. Furthermore, lower activation energy of ~ 0.94 eV is displayed due to the avoidance of La_2GeO_5.

Acknowledgements

The authors are grateful for the financial support from the National Natural Science Foundation of China (No. 11074089 and 51172087), Specialized Research Fund for the Doctoral Program of Higher Education (No. 20110061110011), National Basic Research Program of China (No. 2011CB808204) and Scientific Research Foundation for the Returned Overseas Chinese Scholars, State Education Ministry.

Notes and references

State Key Laboratory of Superhard Materials, Jilin University, Changchun, 130012, China. Fax: +86 431 85168346; Tel: +86 431 85168346; E-mail: gwei@jlu.edu.cn

1 E. Kendrick, J. Kendrick, K. S. Knight, M. S. Islam and P. R. Slater, *Nature Mater.*, 2007, **6**, 871-875.
2 L. Malavasi, C. A. J. Fisher and M. S. Islam, *Chem. Soc. Rev.*, 2010, **39**, 4370-4387.
3 M. Santos, C. Alves, F. A. C. Oliveira, T. Marcelo, J. Mascarenhas, A. Cavaleiro and B. Trindade, *J. Power Sources*, 2013, **231**, 146-152.
4 W. Gao, H. L. Liao and C. Coddet, *Appl. Surf. Sci.*, 2008, **254**, 5548-5551.
5 T. Matsui, A. Mineshige, T. Funahashi, H. Mieda, Y. Daiko, M. Kobune, H. Yoshioka and T. Yazawa, *J. Power Sources*, 2012, **217**, 170-174.
6 I. Santacruz, J. M. Porras-Vazquez, E. R. Losilla and M. A. G. Aranda, *J. Eur. Ceram. Soc.*, 2011, **31**, 1573-1580.
7 D. Marrero-Lopez, P. Diaz-Carrasco, J. Pena-Martinez, J. C. Ruiz-Morales and J. R. Ramos-Barrado, *Fuel Cells*, 2011, **11**, 65-74.
8 X. Wu, D. landheer, T. Quance, M. J. Graham and G. A. Botton, *Appl. Surf. Sci.*, 2002, **15**, 15-20.
9 P. M. Panchmatia, A. Orera, E. Kendrick, J. V. Hanna, M. E. Smith, P. R. Slater and S. Islam, *J. Mater. Chem.*, 2010, **20**, 2766-2772.
10 E. Jothinathan, K. Vanmeensel and J. Vleugels, *J. Eur. Ceram. Soc.*, 2010, **30**, 1699-1706.
11 W. Gao, H. L. Liao and C. Coddet, *J. Power Sources*, 2008, **179**, 739-744.
12 J. R. Tolchard, P. R. Slater and M. S. Islam, *Adv. Funct. Mater.*, 2007, **17**, 2564-2571.
13 A. Vincent, S. B. Savignat and F. Gervais, *J. Eur. Ceram. Soc.*, 2007, **27**, 1187-1192.
14 G. C. Yin, H. Yin, H. Y. Zhu, X. X. Wu, L. H. Zhong, M. L. Sun, R. D. Cong, J. Zhang , W. Gao and Q. L. Cui, *Jouranl of Alloys and Compounds*, 2014, **586**, 279-284.
15 P. Desclaux, S. Nurnberger, M. Rzepka and U. Stimming, *Int. J. Hydrogen Energy*, 2011, **36**, 10278-10281.
16 E. Courtin, P. Boy, T. Piquero, J. Vulliet, N. Poirot and C. Laberty-Robert, *J. Power Sources*, 2012, **206**, 77-83.
17 T. Ishihara, H. Matsuda and Y. Takita, *J. Am. Chem. Soc.*, 1994, **116**, 3801-3803.
18 E. Bechade, O. Masson, T. Iwata, I. Julien, K. Fukuda, P. Thomas and E. Champion, *Chem. Mater.*, 2009, **21**, 2508-2517.
19 B. Li, W. Liu and W. Pan, *J. Power Sources*, 2010, **195**, 2196-2201.
20 K. Fukuda, T. Asaka, N. Ishizawa, H. Mino, D. Urushihara, H. Mino, D. Urushihara, A. Berghout, E. Bechade, O. Masson, I. Julien and P. Thomas, *Chem. Mater.*, 2012, **24**, 2611-2618.

21 F. Sun, N. N. Zhang, J. L. Li and H. L. Liao, *J. Power Sources*, 2013, **223**, 36-41.
22 E. Kendrick, J. E. H. Sansom, J. R. Tolchard, M. S. Islam and P. R. Slater, *Faraday Discuss.*, 2007, **134**, 181-194.
23 E. J. Abram, C. A. Kirk, D. C. Sinclair and A. R. West, *Solid State Ionics*, 2005, **176**, 1941-1947.
24 J. R. Tolchard, J. E. H. Sansom, P. R. Sansom and M. S. Islam, *J. Solid State Electrochem.*, 2004, **8**, 668-673.
25 E. Kendrick, D. Headspith, A. Orera, D. C. Apperley, R. I. Smith, M. G. Francesconi and P. R. Slater, *J. Mater. Chem.*, 2009, **19**, 749-754.
26 J. E. H. Sansom, L. Hildebrandt and P. R. Slater, *Ionics*, 2002, **8**, 155-160.
27 C. G. Tian, J. L. Liu, C. J. Guo, J. Cai, T. X. Cai and Y. W. Zeng, *J. Alloys Compd.*, 2008, **60**, 646-650.
28 E. Rodriguez-Reyna, A. F. Fuentes, M. Maczka, J. Hanza, K. Boulahya and U. Amador, *Solid State Sciences*, 2006, **8**, 168-177.
29 Z. X. Huang, B. Y. Li and J. Liu, *Phys. Status Solidi*, 2010, **207**, 2247-2251.
30 B. Y. Li, J. Liu, Y. X. Hu and Z. X. Huang, *Journal of Alloys and Compounds*, 2011, **509**, 3172-3176.
31 H. C. Yao, J. S. Wang, D. G. Hu, J. F. Li, X. R. Lu and Z. J. Li, *Solid State Ionics*, 2010, **181**, 41-47.
32 L. Leon-Reina, M. C. Martin-Sedeno, E. R. Losilla, A. Cabeza, M. Martinez-Lara, S. Bruque, F. M. B. Marques, D.V. Sheptyakov and M. A. G. Aranda, *Chem. Mater.*, 2003, **15**, 2099-2108.
33 G. C. Yin, H. Yin, L. H. Zhong, M. L. Sun, J. K. Zhang, X. J. Xie, R. D. Cong, X. Wang, W. Gao and Q. L. Cui, *Chin. Phys. B*, 2014, **23**, 048202.
34 B. H. Toby, *Powder Diff.*, 2006, **21**, 67-70.
35 J. E. H. Sansom and P. R. Slater, *Solid State Ionics*, 2004, **167**, 23-27.
36 J. E. H. Sansom, A. Najib and P. R. Slater, *Solid State Ionics*, 2004, **175**, 353-355.
37 K. Fukuda, T. Asaka, R. Hamaguchi, T. Suzuki, H. Oka, A. Berghout, E. Bechade, O. Masson, I. Julien, E. Champion and P. Thomas, *Chem. Mater.*, 2011, **23**, 5474-5483.
38 K. Fukuda, T. Asaka, S. Hara, M. Oyabu, A. Berghout, E. Bechade, O. Masson, I. Julien and P. Thomas, *Chem. Mater.*, 2013, **25**, 2154-2162.
39 J. Xiang, Z. G. Liu, J. H. Ouyang and F. Y. Yan, *Electrochimica Acta*, 2012, **65**, 251-256.